INTERNATIONAL JOURNAL FOR NUMERICAL METHODS IN ENGINEERING
Int. J. Numer. Meth. Engng 2009; **78**:1–31
Published online 6 November 2008 in Wiley InterScience (www.interscience.wiley.com). DOI: 10.1002/nme.2476

Explicit coupled thermo-mechanical finite element model of steel solidification

Seid Koric*, †, Lance C. Hibbeler and Brian G. Thomas

National Center for Supercomputing Applications—NCSA, Mechanical Science and Engineering Department, University of Illinois at Urbana-Champaign, 1205 W. Clark Street, Urbana, IL 61801, U.S.A.

SUMMARY

The explicit finite element method is applied in this work to simulate the coupled and highly non-linear thermo-mechanical phenomena that occur during steel solidification in continuous casting processes. Variable mass scaling is used to efficiently model these processes in their natural time scale using a Lagrangian formulation. An efficient and robust local–global viscoplastic integration scheme (*Int. J. Numer. Meth. Engng* 2006; **66**:1955–1989) to solve the highly temperature- and rate-dependent elastic–viscoplastic constitutive equations of solidifying steel has been implemented into the commercial software ABAQUS/Explicit (*ABAQUS User Manuals v6.7.* Simulia Inc., 2007) using a VUMAT subroutine. The model is first verified with a known semi-analytical solution from Weiner and Boley (*J. Mech. Phys. Solids* 1963; **11**:145–154). It is then applied to simulate temperature and stress development in solidifying shell sections in continuous casting molds using realistic temperature-dependent properties and including the effects of ferrostatic pressure, narrow face taper, and mechanical contact. Example simulations include a fully coupled thermo-mechanical analysis of a billet-casting and thin-slab casting in a funnel mold. Explicit temperature and stress results are compared with the results of an implicit formulation and computing times are benchmarked for different problem sizes and different numbers of processor cores. The explicit formulation exhibits significant advantages for this class of contact-solidification problems, especially with large domains on the latest parallel computing platforms. Copyright © 2008 John Wiley & Sons, Ltd.

Received 17 March 2008; Revised 13 August 2008; Accepted 28 August 2008

KEY WORDS: explicit; thermal stress; finite element; solidification; continuous casting; parallel computational benchmarks; ABAQUS

*Correspondence to: Seid Koric, National Center for Supercomputing Applications—NCSA, Mechanical Science and Engineering Department, University of Illinois at Urbana-Champaign, 1205 W. Clark Street, Urbana, IL 61801, U.S.A.
†E-mail: skoric@ncsa.uiuc.edu

Contract/grant sponsor: National Center for Supercomputing Applications (UIUC)
Contract/grant sponsor: Continuous Casting Consortium at UIUC
Contract/grant sponsor: National Science Foundation; contract/grant number: CMMI-07-27620
Contract/grant sponsor: Corus Steel in IJmuiden, The Netherlands

1. INTRODUCTION

Commercial processes involving solidification are worthy applications for advanced computational models because they are mature processes that are difficult to improve further through empirical means and also involve harsh environments that make experimentation difficult. A major obstacle to successful modeling is the time-consuming nature of these computationally demanding problems. This is due to the many coupled, highly non-linear phenomena involved, their multi-dimensional nature, and the refined meshes needed to obtain reasonable accuracy.

Continuous casting has produced 85% or more of the steel in the world for several decades. The molten steel from the extraction processes flows under gravity into a bottomless copper mold. Molds range in shape from simple square billets to complex beam-blanks or funnel shapes. The steel solidifies a skin or 'shell' against the water-cooled mold walls, and is pulled from the bottom of the mold at a specified 'casting speed' that matches the solidification rate such that the process appears steady in a laboratory frame of reference. The few seconds the steel spends in the mold are critical, as most of the defects in the final product arise in the mold [1]. Stresses and strains caused by thermal contraction, interaction with the mold walls, or other mechanical forces can generate internal cracks that can lead to catastrophic breakouts, or fill with segregated liquid and cause permanent defects in the final product. The quality of continuously cast products is constantly improving, but better modeling work is needed to quantitatively understand how defects form in order to maximize quality and productivity.

Many obstacles arise during the numerical modeling of thermo-mechanical behavior in solidification processes like continuous casting. These obstacles include the incorporation and integration of the highly non-linear viscoplastic constitutive laws, treatment of latent heat, treatment of the liquid/mushy zone that involves composition-dependent segregation, temperature-dependent material properties, intermittent contact between the solidified shell and mold surfaces, and coupling between the heat transfer and stress analysis through the changing thickness of the shell–mold interfacial gap.

Various numerical methods have been used to solve the equations that govern the thermo-mechanical behavior of a solidifying body. Hattel *et al.* [2] applied a finite-difference method to simulate three-dimensional (3D) thermo-elastic stresses in a die casting with simple geometry. Taylor *et al.* [3] have developed a finite volume code with unstructured meshes to model various casting processes. Lee and coworkers [4] recently developed a finite volume method for coupled fluid flow, heat transfer, and stress of solidifying shells in a beam-blank mold. Nevertheless, almost all thermo-mechanical models of solidification processes have applied finite element methods with implicit solution methods [5–20]. This is due to their efficiency over finite-difference and finite volume methods in fast, stable convergence of the highly coupled and stiff non-linearities typically encountered in stress problems, especially with complex geometries.

When fluid flow in the liquid pool must be coupled together with mechanical behavior in the solidifying shell, a few recent papers have adopted an arbitrary Lagrangian Eulerian (ALE) formulation [15–17]. This implicit method combines Lagrangian elements, which move with the material, together with Eulerian elements, which remain fixed in space while material 'flows' through them. Bellet and Fachinotti [15] integrated ALE in the liquid and mushy regions with a pure Lagrangian treatment of solid regions in developing a combined model of mold filling and thermo-mechanical solidification. In ALE mushy regions, the nodes contain both solid (Lagrangian) and liquid (Eulerian) velocities (displacement rates). The full set of equations, including both velocity and pressure,

DOI: 10.1002/nme

are linearized and solved at each time step using implicit Newton–Raphson (NR) iterations, with the aid of a preconditioned iterative solver. Despite the modeling advantages of a single simulation that combines fluid flow, solidification, and mechanical behavior, the practical application of this method is hampered by its complexity, its need for 3D remeshing procedures, and convergence problems. Furthermore, extra complexity is needed to account for the advection of material through the computational grid and to update the associated time-dependent variables. Risso *et al.* [16] found that an ALE axisymmetric model of a billet casting had a higher computational cost than a pure Lagrangian generalized plane strain model and recommended the latter for future research work.

The vast majority of previous solidification models have adopted implicit finite element analysis in a Langrangian frame of reference, by tracking a slice through the strand as it moves down the caster, within a variety of one- and two-dimensional (1D and 2D) domains [5–14, 18, 19], and a recent uncoupled analysis with a 3D domain [20]. Although Lagrangian elements sometimes experience distortion problems when the material is severely deformed, this is not an issue in the solid and mushy regions of castings. In solidification problems, cracks will form if the strains exceed only a few percent, so a small-strain model can be accurately applied to investigate thermal–mechanical behavior up to the initiation of cracks. Cracks can be predicted with these models with the aid of damage criteria [19]. Furthermore, the advective terms and history-dependent variable(s) can be easily updated with Langrangian elements. Care must be taken in liquid regions to allow volumetric flow while avoiding excessive strain.

Numerous constitutive models have been used to simulate solidification stresses, starting with simple elastic–plastic models [6, 7]. A separate creep model can be added to roughly account for the time dependency [8]. More accurate elastic–viscoplastic models have been used [1, 5, 9–20], which unify the phenomena of creep and plasticity together through a structure parameter such as inelastic strain in the solid. Integration of these time-dependent constitutive laws is a very challenging computational task due to their numerical stiffness. Koric and Thomas [5] implemented a robust local viscoplastic integration scheme from an in-house code CON2D [1, 12, 13] into the commercial implicit finite element package ABAQUS/Standard via its user-defined material subroutine UMAT, which has opened the door for realistic large-scale uncoupled 3D computational modeling of complex-solidification processes [20]. However, coupled 3D problems with reasonable mesh resolution are still difficult to solve, owing to memory and speed limitations, even on supercomputers.

For over 15 years, finite element methods with explicit time integration have been used efficiently to simulate dynamic processes involving severe non-linearities, such as sheet-forming, forging, and rolling [21–23]. Rebelo *et al*. [24] and recently Harewood and McHugh [25] found the explicit method to be more efficient and robust than the implicit method for large quasi-static problems with combined non-linearities from complex material models and difficult contact conditions. Explicit methods have not previously been applied to thermo-mechanical analysis of solidification.

The objective of this work is to develop an effective and efficient tool to realistically model thermo-mechanical behavior in large solidification problems involving complex interacting phenomena, and to evaluate its performance. To do this, a novel approach is proposed here to link a cost-effective explicit time integration solution method on the global level with an efficient and robust local viscoplastic integration scheme. Both the thermal stress results and the computational performance are compared with previous implicit methods. The effects of problem size and parallel processing are also investigated.

DOI: 10.1002/nme

2. GOVERNING EQUATIONS AND SOLUTION METHODS

The transient energy equation [26] is given as follows:

$$\rho\left(\frac{\partial H(T)}{\partial t}\right)=\nabla\cdot(k(T)\nabla T) \tag{1}$$

along with boundary conditions of prescribed temperature, prescribed heat flux, or the following convection condition:

$$(-k\nabla T)\cdot\mathbf{n}=h_g(T-T_{\mathrm{m}}) \tag{2}$$

where ρ is the density, k is the isotropic temperature-dependent thermal conductivity, H is the temperature-dependent enthalpy, which includes the latent heat of solidification, h_g is an effective heat transfer coefficient at boundary portion A_h, T_{m} is the mold surface temperature, and $\mathbf{n}$ is the unit vector normal to the boundary.

The mechanical behavior of a material during solidification is controlled largely by the strains, which must remain lower than a few percent to avoid cracking [27]. Assuming small strain, as confirmed in many previous solidification models [8, 12, 13, 16], the linearized strain tensor is [28]

$$\boldsymbol{\varepsilon}=\tfrac{1}{2}[\nabla\mathbf{u}+(\nabla\mathbf{u})^{\mathrm{T}}] \tag{3}$$

The statement of mechanical equilibrium is then

$$\nabla\cdot\boldsymbol{\sigma}(\mathbf{x})+\mathbf{b}=0 \tag{4}$$

where $\boldsymbol{\sigma}$ is the Cauchy stress tensor and $\mathbf{b}$ is the body force density vector. Together with boundary conditions of prescribed displacements or surface tractions $\boldsymbol{\sigma}\cdot\mathbf{n}=\boldsymbol{\Phi}$ on boundary portion A_Φ, Equation (4) defines a quasi-static boundary value problem. The rate representation of the total strain used in this elastic–viscoplastic model is given by

$$\dot{\boldsymbol{\varepsilon}}=\dot{\boldsymbol{\varepsilon}}_{\mathrm{el}}+\dot{\boldsymbol{\varepsilon}}_{\mathrm{ie}}+\dot{\boldsymbol{\varepsilon}}_{\mathrm{th}} \tag{5}$$

where $\dot{\boldsymbol{\varepsilon}}_{\mathrm{el}}, \dot{\boldsymbol{\varepsilon}}_{\mathrm{ie}}, \dot{\boldsymbol{\varepsilon}}_{\mathrm{th}}$ are the elastic, inelastic (plastic+creep), and thermal strain rate tensors, respectively, and the superposed dot represents the first time derivative. Stress rate $\dot{\boldsymbol{\sigma}}$ depends on elastic strain rate and with negligible large rotations, which is given by Equation (6) in which ':' represents inner tensor product.

$$\dot{\boldsymbol{\sigma}}=\underline{\underline{\mathbf{D}}}:(\dot{\boldsymbol{\varepsilon}}-\dot{\boldsymbol{\varepsilon}}_{\mathrm{ie}}-\dot{\boldsymbol{\varepsilon}}_{\mathrm{th}}) \tag{6}$$

$\underline{\underline{\mathbf{D}}}$ is the fourth-order isotropic elasticity tensor given by Equation (7), which neglects the slightly anisotropic behavior of solidified metal with large oriented, columnar grains:

$$\underline{\underline{\mathbf{D}}}=2\mu\underline{\underline{\mathbf{I}}}+(k_{\mathrm{B}}-\tfrac{2}{3}\mu)\mathbf{I}\otimes\mathbf{I} \tag{7}$$

Here, μ and k_{B} are the shear modulus and bulk modulus, and are in general functions of temperature, while $\underline{\underline{\mathbf{I}}}$ and $\mathbf{I}$ are the fourth- and second-order identity tensors, respectively, and '$\otimes$' denotes outer tensor product.

DOI: 10.1002/nme

2.1. *Implicit finite element method*

In the implicit non-linear finite element solution procedure, the fully implicit 'backward finite-difference' algorithm is applied for time integration of the governing equations. In each time step Δt, the thermal field is solved, and then the resulting thermal strains are used to solve the mechanical problem. Iteration continues until tolerances on residual errors for both equation systems are satisfied before proceeding to the next time step, as shown in Figure 1. Within each time step, each non-linear equation system is linearized and solved with a full NR iteration scheme, which requires several 'global equilibrium iterations' (subscript i) as follows:

$$[K_{i-1}^{t+\Delta t}]\{\Delta u_{i-1}^{t+\Delta t}\} = \{R_{i-1}^{t+\Delta t}\} \tag{8}$$

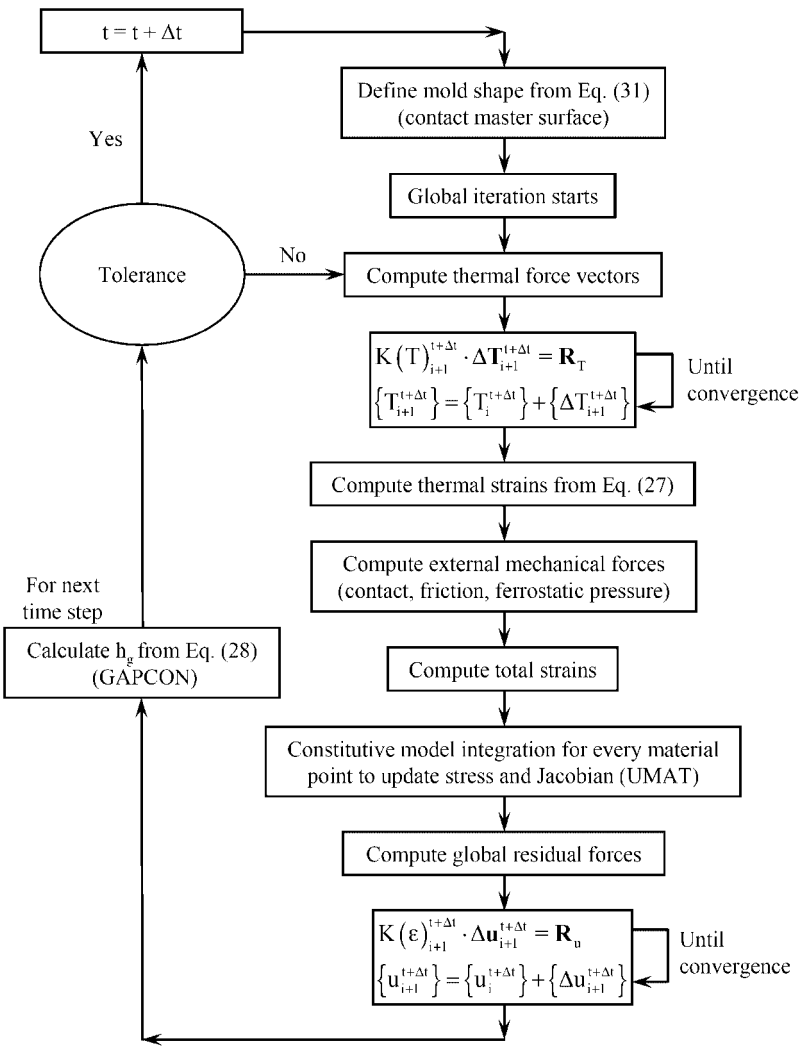

Figure 1. Implicit solution flow chart.

DOI: 10.1002/nme

where $\{\Delta u_{i-1}^{t+\Delta t}\}$ is the incremental change to the solution vector (temperatures in thermal problems and displacements in mechanical problems) and $\{R_{i-1}^{t+\Delta t}\}$ is the residual error vector. Equation (8) is solved for $\{\Delta u_{i-1}^{t+\Delta t}\}$, which is used to update the solution vector in Equation (9), until convergence is achieved everywhere at time $t+\Delta t$ (when the update vector is sufficiently small).

$$\{u_i^{t+\Delta t}\} = \{u_{i-1}^{t+\Delta t}\} + \{\Delta u_{i-1}^{t+\Delta t}\} \tag{9}$$

The tangent stiffness matrix $[K^{t+\Delta t}]$ is defined in Equation (11) from the consistent tangent operator, also known as the 'material Jacobian,' [J], which is defined in Equation (10) for mechanical problems, taking $\Delta\hat{\varepsilon}^{t+\Delta t}$ as a 'guessed' mechanical strain increment, based on the current best displacement increment.

$$\underline{\underline{\mathbf{J}}} = \frac{\partial \Delta \boldsymbol{\sigma}^{t+\Delta t}}{\partial \Delta \hat{\boldsymbol{\varepsilon}}^{t+\Delta t}} \tag{10}$$

$$[K^{t+\Delta t}] = \int_V [B]^{\mathrm{T}}[J][B]\,\mathrm{d}V \tag{11}$$

where $[B] = \partial[N]/\partial\mathbf{x}$ contains the spatial derivatives of the element shape functions $[N]$.

The finite element approximation of thermal problem, Equation (1), is given by

$$\frac{1}{\Delta t}\int_V [N]^{\mathrm{T}}\rho(H^{t+\Delta t} - H^t)\,\mathrm{d}V + \int_V [B]^{\mathrm{T}}k(T)[B]\,\mathrm{d}V - \int_{A_h} [N]^{\mathrm{T}}h_g(T - T_m)\,\mathrm{d}A = 0 \tag{12}$$

Applying the NR-iteration scheme gives the following linearized matrix equation:

$$\left[\frac{1}{\Delta t}\int_V [N]^{\mathrm{T}}\rho\left(\frac{\mathrm{d}H}{\mathrm{d}T}\right)_i^{t+\Delta t}[N]\,\mathrm{d}V + \int_V [B]^{\mathrm{T}}k_i^{t+\Delta t}[B]\,\mathrm{d}V - \int_{A_h}[N]^{\mathrm{T}}h_g^t[N]\,\mathrm{d}A\right]\{\Delta T_{i+1}^{t+\Delta t}\}$$

$$= \{R_T\} = \int_{A_h}[N]^{\mathrm{T}}h_g^t(T_i^{t+\Delta t} - T_m)\,\mathrm{d}A$$

$$-\frac{1}{\Delta t}\int_V [N]^{\mathrm{T}}\rho(H_i^{t+\Delta t} - H^t)\,\mathrm{d}V - \int_V [B]^{\mathrm{T}}k^t[B]\,\mathrm{d}V \tag{13}$$

For the mechanical problem, the residual error is defined as the imbalance between the force vector from internal stresses, $\{S^t\}$ and the externally applied loads, $\{P^t\}$ from body forces and surface tractions, [5, 29]:

$$\{R_u^t\} = \{S^t\} - \{P^t\} = \int_V [B]^{\mathrm{T}}\{\sigma^t\}\,\mathrm{d}V - \left(\int_V [N]^{\mathrm{T}}\{b^t\}\,\mathrm{d}V + \int_{A_\Phi}[N]^{\mathrm{T}}\{\Phi^t\}\,\mathrm{d}A\right) \tag{14}$$

Coupling between the thermal and mechanical fields is enforced in this work with similar accuracy to the 'staggered' or 'separated' solution approach [30]. Further details on this method is provided elsewhere [5].

2.2. *Explicit finite element method*

In addition to using an explicit method for both time and spatial integration, the explicit finite element method used here differs notably from previous methods in that the mechanical governing

DOI: 10.1002/nme

equation adds an inertial term $\rho\ddot{\mathbf{u}}$ to the right-hand side of Equation (3), where $\ddot{\mathbf{u}}$ is the acceleration vector. The heat transfer problem is simply marched through time by integrating Equation (1) using the fully explicit 'forward finite-difference' method

$$\{T\}^{t+\Delta t} = \{T\}^t + \{\dot{T}\}^t \Delta t \tag{15}$$

The values of $\{\dot{T}\}^t$ are computed after standard finite element assembly as follows:

$$\{\dot{T}\}^t = [C]^{-1} \left(\int_{A_h} [N]^{\mathrm{T}} h_g (T - T_m)\, \mathrm{d}A - \int_V [B]^{\mathrm{T}} k [B]\, \mathrm{d}V \{T\}^t \right) \tag{16}$$

where $[C]$ is the lumped thermal capacitance matrix based on the previous time step, which is inverted analytically, thus enabling an explicit solution of Equation (16)

$$[C] = \int_V [N]^{\mathrm{T}} \rho \left(\frac{\mathrm{d}H}{\mathrm{d}T} \right)^t [N]\, \mathrm{d}V \tag{17}$$

The numerical stability limit for the forward-difference operator in the thermal solution is given by

$$\Delta t \leqslant \min \left(\frac{\rho c_p L_e^2}{2k} \right) \tag{18}$$

where k is the thermal conductivity, ρ is the density, and specific heat c_p is found from the slope of the enthalpy-temperature data, except in the solidification region, where c_p is found using [26]

$$c_p(T) = \frac{\mathrm{d}H}{\mathrm{d}T} - \frac{H_{\mathrm{f}}}{(T_{\mathrm{liq}} - T_{\mathrm{sol}})} \tag{19}$$

where H_{f} is the latent heat of solidification and T_{liq} and T_{sol} are the liquidus and solidus temperatures.

The mechanical problem is formulated in terms of nodal accelerations and explicitly advances the kinematic state of the system from the previous time step without iteration. At the beginning of a time step, dynamic equilibrium is solved:

$$\{\ddot{u}^t\} = [M]^{-1} (\{P\}^t - \{S\}^t) \tag{20}$$

where $[M]$ is the diagonal 'lumped' nodal mass matrix, which is trivial to invert, and $\{\ddot{u}^t\}$ are the nodal accelerations at the beginning of the increment. The accelerations are integrated explicitly through time using the central-difference method, which calculates the change in velocity assuming constant acceleration over a small time step. This velocity change is added to the velocity from the middle of the previous step to calculate the velocities at the middle of the current step:

$$\{\dot{u}^{t+\Delta t/2}\} = \{\dot{u}^{t-\Delta t/2}\} + \frac{(\Delta t^{t+\Delta t} + \Delta t^t)}{2} \{\ddot{u}^t\} \tag{21}$$

The velocities are integrated once more to calculate the displacement increment, which is then used to update the displacements at the end of the time step:

$$\{u^{t+\Delta t}\} = \{u^t\} + \Delta t^{t+\Delta t} \{\dot{u}^{t+\Delta t/2}\} \tag{22}$$

DOI: 10.1002/nme

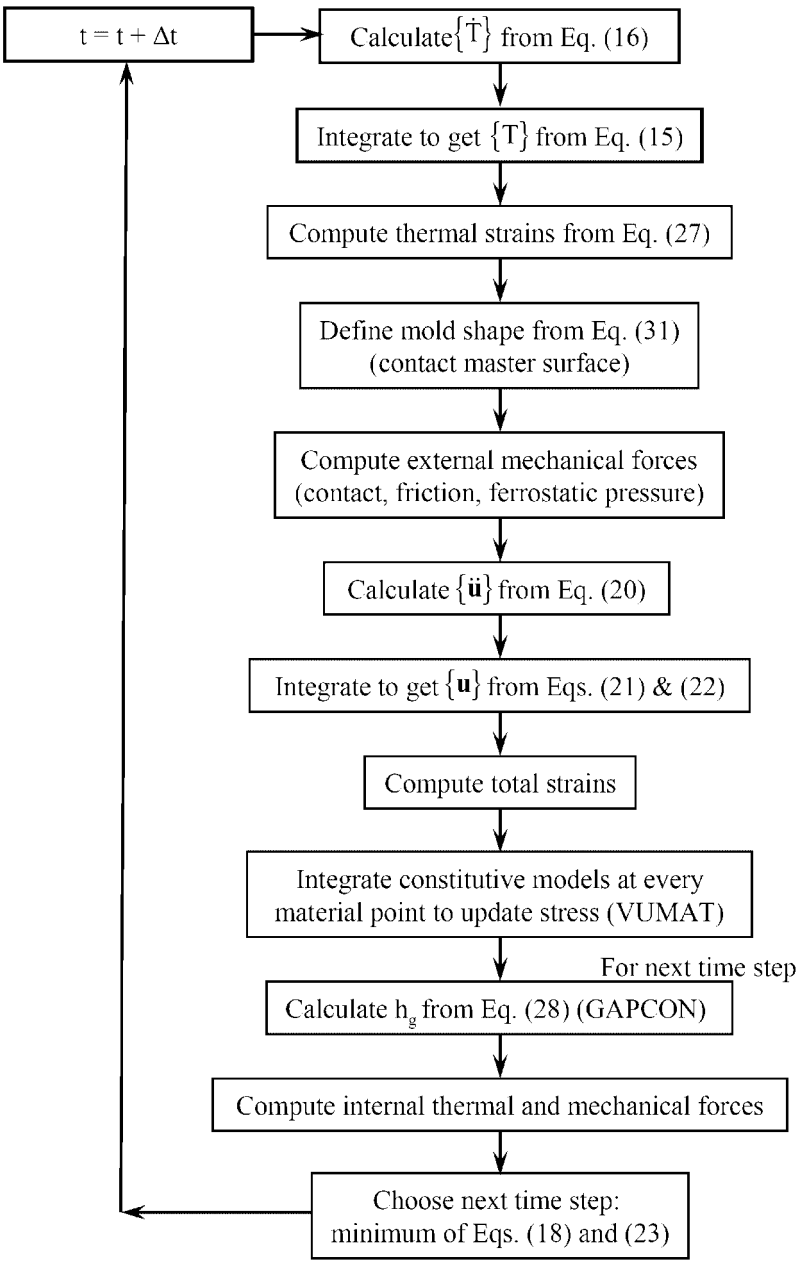

Figure 2. Explicit solution flow chart.

A numerical stability requirement limits the maximum time step size in the explicit method. In general, the critical time step is $\Delta t \leqslant 2/\omega_{\max}$, where $\omega_{\max}$ is the highest frequency (largest eigenvalue) of the system. To avoid extracting eigenvalues, a more practical estimate of the stability

DOI: 10.1002/nme

limit is made using the dilatational wave speed c_d and the characteristic length L_e of the smallest element in the domain:

$$\Delta t \leqslant \min\left(\frac{L_e}{c_d}\right) \tag{23}$$

$$c_d = \sqrt{\frac{\lambda+2\mu}{\rho}} \tag{24}$$

where λ is the first Lamé constant, μ is the shear modulus, and ρ is the density of the element, which is chosen automatically to satisfy the user-defined critical time step. Despite the large number of time steps needed for the explicit method, it is often more efficient than the implicit method, particularly when many expensive NR iterations are needed to solve Equation (8). Also, contact conditions are solved more easily using this explicit method than using an implicit method [24, 25]. Furthermore, complete coupling between the temperature and displacement fields is obtained automatically, given that the explicit method does not require iteration at the global level. The flowchart in Figure 2 details the steps in this explicit method.

In problems where inertial effects are not important, such as solidification, the density in Equation (24) can be used as a parameter in the explicit analysis to reduce computational costs. Specifically, increasing the density, called 'mass scaling', allows larger time steps without introducing stability problems. This adds stability by damping the inconsequential stress shock waves that propagate rapidly throughout the metal. The density increases are permissible because the shock waves are still fast enough after damping to equilibrate the stresses and have negligible effect on the results. Equation (24) shows that this approach can reduce solution time in proportion to the square root of the factor by which density was increased. Because the stiffness properties change drastically during solidification, mass scaling was adjusted periodically during the analysis, while maintaining the user-defined desired time step [31]. It was insured throughout this work (as verified during post-processing) that changes in the mass and consequent increases in the inertial forces do not alter the solution, by choosing the time step to keep the ratio of the kinetic energy to the total strain energy less than 5% [25].

3. NUMERICAL MODEL VERIFICATION

A semi-analytical solution of thermal stresses in an unconstrained, elasto-plastic solidifying plate [32] was used to verify both the implicit and explicit computational models. Taking advantage of the large length and width of the solidification test problem, a 1D solution with a generalized plane strain condition in both the y and z directions can produce the complete 3D stress and strain states [5, 13].

The domain adopted for this problem consists of a thin, narrow 30×0.1 mm slice through the plate thickness as shown in Figure 3. For the thermal analysis, the 1D transient heat conduction equation is solved, as described elsewhere [5, 13]. The surface temperature drops instantly from a constant initial temperature (which includes a very small superheat) to a fixed temperature at the mold wall, according to the conditions and properties given in Table I. A very narrow mushy region, 0.1°C, is used to approximate the single melting temperature assumed in this problem, to model pure materials and eutectic alloys. The material in the mechanical problem exhibits

DOI: 10.1002/nme

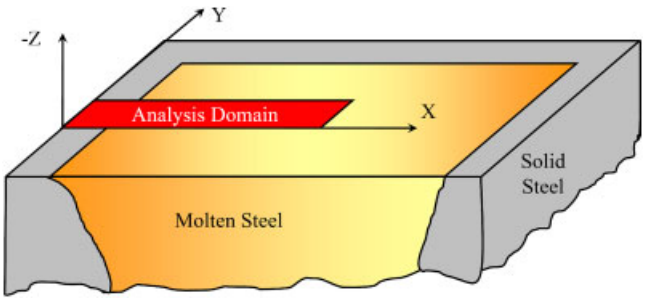

Figure 3. Solidifying slice.

Table I. Constants used in solidification test problem.

Thermal conductivity	33.0	W/(m K)
Specific heat	661.0	J/(kg K)
Elastic modulus in solid	40.0	GPa
Elastic modulus in liquid	14.0	GPa
Thermal linear expansion coefficient	20.0×10^{-6}	1/K
Density	7500.0	kg/m^3
Poisson ratio	0.3	—
Liquidus temperature	1494.45	°C
Solidification temperature (analytical)	1494.4	°C
Solidus temperature	1494.35	°C
Initial temperature	1495.0	°C
Latent heat	272.0	kJ/kg
Surface temperature	1000.0	°C

elastic-perfectly plastic constitutive behavior. The yield stress drops linearly with temperature from 20 MPa at 1000°C (the surface temperature) to zero at the melting temperature, which was approximated in the numerical models by $\sigma_Y = 0.03$ MPa at the solidus temperature 1494.4°C. All other material properties are constant with temperature. Further details on this particular analytical solution are given elsewhere [5, 13].

The implicit domain consists of a single row of 2D generalized plane strain elements (in the x–y plane), with the condition of constant strain imposed in the z direction. In addition, a second generalized plane strain condition was imposed in the y direction by coupling the displacements of all nodes along one edge of the slice domain. ABAQUS/Explicit does not currently support generalized plane strain elements, so 3D eight-node hexahedron elements were used instead. The generalized plain strain condition in the z direction was enforced by fixing the z-displacements to zero on the bottom surface of the domain and coupling the z-displacements of the nodes on the top surface of the domain. The y direction generalized plane strain condition was similarly enforced. Using fully integrated elements ($2 \times 2 \times 2$ Gauss–Legendre quadrature) in the explicit model resulted in underprediction of the surface stress, and selecting reduced-integration elements (one integration point, standard hour-glass control, and average-strain kinematic splitting) ameliorated this problem.

Figures 4 and 5 show the temperature and the stress distributions, respectively, across the solidifying shell at two different times. These figures compare the semi-analytical solution with the

DOI: 10.1002/nme

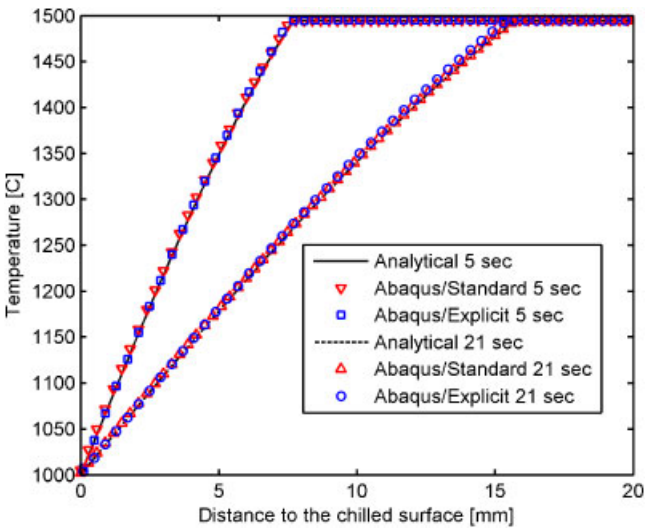

Figure 4. Model verification temperature results.

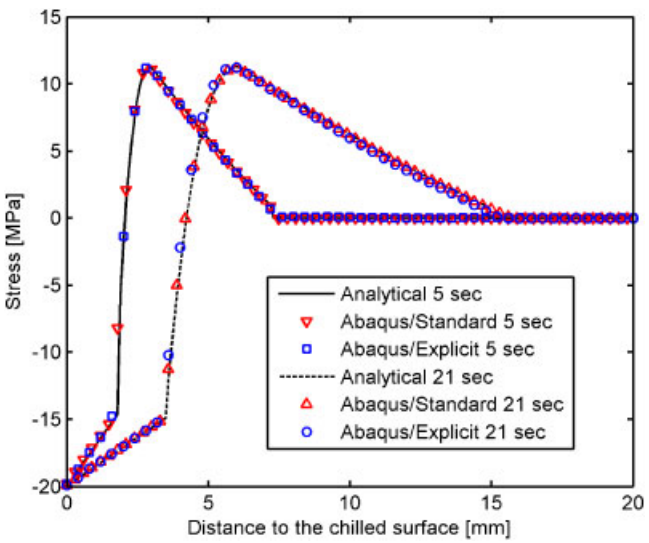

Figure 5. Model verification stress results.

numerical solutions from both the implicit and explicit models. The temperature and stress results match very well among the all three methods. More details about verification of the implicit model can be found elsewhere [5] including comparisons with other less-efficient integration methods and a convergence study.

In the absence of mass scaling, the explicit model requires a very small time step. Given the 0.1-mm-square elements, the first Lamé constant $\lambda = vE/(1+v)(1-2v) = 8.077\,\text{GPa}$, and shear

DOI: 10.1002/nme

modulus $\mu = E/2(1+\nu) = 5.385\,\text{GPa}$, Equations (23) and (24) provide that the critical time step is 63.1×10^{-9} s. Setting the user-defined maximum time step to be 10^{-4} s (and thus forcing a density increase by a factor of about 2.5×10^6) did not produce any significant change in the temperature or stress results in the explicit model.

4. MODELING OF CONTINUOUS CASTING OF STEEL

The steel grade simulated in this work is a mild carbon steel with 0.27 wt% C and a handful of other trace elements, giving solidus and liquidus temperatures of 1411.79 and 1500.7°C, respectively. Given the large temperature range the material undergoes in the continuous casting process, the temperature- and composition-dependence of many thermo-physical properties and phenomena must be taken into account, most notably the viscoplastic high-temperature constitutive laws, but also material properties. Other phenomena specific to the continuous casting process are also treated in this section.

4.1. Constitutive models and their integration

This work solves separate constitutive models for the delta-ferrite and austenite solid phases, which have been shown in previous work to accurately reproduce the temperature, strain-rate, and composition-dependent behavior of solidifying steel [33]. The rate-dependent, elastic–viscoplastic model III of Kozlowski *et al.* [34] given in Equation (25) was chosen for the austenite phase of solidifying plain-carbon steels. This model was developed to match tensile test measurements of Wray [35] and creep test data of Suzuki and Tacke [36].

$$\dot{\bar{\varepsilon}}_{\text{ie}}[(\text{s})^{-1}] = f_{\text{C}}(\bar{\sigma}(\text{MPa}) - f_1 \bar{\varepsilon}_{\text{ie}} |\bar{\varepsilon}_{\text{ie}}|^{f2-1})^{f3} \exp\left(-\frac{Q}{T(K)}\right) \tag{25}$$

where Q is the 44 465 K; f_1 is $130.5 - 5.128 \times 10^{-3} T(\text{K})$; f_2 is $-0.6289 + 1.114 \times 10^{-3} T(\text{K})$; f_3 is $8.132 - 1.54 \times 10^{-3} T(\text{K})$; and f_{C} is $46\,550 + 71\,400(\%\text{C}) + 120\,000(\%\text{C})^2$.

This empirical relation relates the equivalent inelastic strain rate $\dot{\bar{\varepsilon}}_{\text{ie}}$ with the von Mises stress $\bar{\sigma}$, equivalent inelastic strain $\bar{\varepsilon}_{\text{ie}}$, activation energy constant Q, carbon content %C, and several empirical temperature- or steel-grade-dependent constants $f_1, f_2, f_3, f_{\text{C}}$. Constant Q (in Kelvin) is the ratio of activation energy 369 kJ/mol, which is found to be close to that of self-diffusion of austenite iron [37], and the universal gas constant 8.31 J/(mol K).

The modified power-law model developed by Zhu [12], Equation (26), was used to simulate the delta-ferrite phase, which exhibits significantly higher creep rates and lower strength than the austenite phase

$$\dot{\bar{\varepsilon}}_{\text{ie}}(\text{s})^{-1} = 0.1 \left| \frac{\bar{\sigma}(\text{MPa})}{f_{\delta\text{c}}(\%\text{C}) \left(\dfrac{T(\text{K})}{300}\right)^{-5.52} (1 + 1000\bar{\varepsilon}_{\text{ie}})^m} \right|^n \tag{26}$$

where $f_{\delta\text{c}}(\%\text{C})$ is the $1.3678 \times 10^4 (\%\text{C})^{-5.56 \times 10^{-2}}$; m is $-9.4156 \times 10^{-5} T(\text{K}) + 0.3495$; and n is $1/1.617 \times 10^{-4} T(\text{K}) - 0.06166$.

DOI: 10.1002/nme

This delta-phase model is applied in the solid whenever the volume fraction of delta ferrite is greater than 10%. This approximates the dominating influence of the very high creep rates in the delta-ferrite phase on the net mechanical behavior of the mixed-phase structure. The calculation of the volume fractions of the liquid, delta, and austenite phases is adopted from previous work [12, 13].

Owing to the highly strain-dependent inelastic responses, a robust integration scheme is required at the local level to integrate the viscoplastic equations over a time step Δt. The system of ordinary differential equations defined at each material point by the viscoplastic model equations (6), (25), and (26) is converted into two 'integrated' scalar equations by the backward-Euler method and then solved using a special bounded NR method [5, 12, 13, 38, 39]. Details of this local integration scheme, implemented originally into the ABAQUS/Standard user subroutine UMAT [5] and here into the ABAQUS/Explicit user subroutine VUMAT, can be found elsewhere [5, 12, 13, 38], along with the derivation of the consistent Jacobian. The explicit formulation naturally does not require the tangent matrix or other complications needed by implicit methods, which is one of the reasons for increased performance. The solution obtained from this 'local' integration step at all material (integration) points is used to update the implicit global finite element equilibrium equations, or the explicit equations, according to the solution procedures explained in Section 2.

4.2. Treatment of liquid and mushy zone

The large property variations between the liquid, mush, and solid phases add a significant challenge to thermo-mechanical simulations. In the current model, an isotropic elastic–perfectly-plastic rate-independent constitutive model is applied above the solidus temperature to ensure negligible strength when liquid is present. This simple fixed-grid approach avoids the difficulties of adaptive meshing or 'giving birth' to solid elements. The liquid yield stress $\sigma_Y = 0.01\,\text{MPa}$ is chosen small enough to effectively eliminate stresses in the liquid and mushy zone, but also large enough to avoid computational difficulties. Local time integration of the liquid and mushy elements uses the standard radial-return algorithm, which is a special form of the backward-Euler procedure [29, 40].

4.3. Thermal strain

Thermal strains arise due to volume changes caused by both temperature differences and phase transformations, including solidification and solid-state phase changes between crystal structures, such as face-centered cubic austenite and body-centered cubic ferrite.

$$\boldsymbol{\varepsilon}_{\text{th}} = \delta_{ij} \int_{T_0}^{T} \alpha(\tau)\, \mathrm{d}\tau \tag{27}$$

where α is the isotropic temperature-dependent coefficient of thermal expansion [5], T_0 is the reference temperature (20°C in this work), T is the temperature of the integration point where α is sought, and δ_{ij} is Kronecker's delta.

4.4. Other thermo-mechanical properties

The temperature-dependence of many material properties of steels has been measured by many experimentalists, such as elastic modulus [41], thermal conductivity [42], specific heat [43], and density [42–44], which is also used to determine the thermal expansion coefficient. The

DOI: 10.1002/nme

measurements have been fitted to temperature- and composition-dependent relations, which can be found elsewhere [13].

4.5. 2D approximation

To simplify the numerical modeling of the continuous casting process, a transient Lagrangian domain is adopted, where the analysis follows a slice of material as it moves down through the casting machine at the casting speed. Relative to a 'laboratory' frame of reference; however, the process reaches steady state after a transient period following the start-up process or a change in casting conditions. For steel, this process has a high Péclet number (typically on the order of 2×10^5), meaning that advection heat transfer dominates over conduction in the axial (casting) direction. Thus, axial conduction can be neglected, and the 2D transient domain can reproduce the complete 3D steady temperature results. For the mechanical analysis, the most appropriate 2D approximation is a generalized plane strain condition, which requires that the axial strain components are all equal to the same constant value (since all model domains in this work take advantage of at least two-fold symmetry).

4.6. Boundary and initial conditions

Continuous casting molds are given a taper to attempt to compensate for the shell shrinkage and ensure good contact (and thus uniform heat transfer) between the shell and the mold. The mold taper and changes in mold shape are included in this numerical model by prescribing the velocities of the mold contact surfaces as a function of time, consistent with distance down the mold according to the Lagrangian formulation used in all of the models. The velocities were prescribed instead of displacements because defining the nodal displacements in the explicit model caused unrealistic behavior from acceleration spikes.

Mechanical contact between the steel shell surfaces and mold surfaces was imposed with a tangential friction factor of 0.1 [45]. The explicit method readily employed the standard 'hard' contact algorithm (penalty-based method) in ABAQUS [31], but the implicit method required some contact stabilization in the form of viscous damping [31] to overcome the contact convergence difficulties experienced in the 3D example, as discussed later.

The heat conducted across the contacting surfaces is a strong function of the distance between the surfaces. The gap between the surfaces is computed in the stress analysis and used in the heat transfer analysis to define conduction across the interface. The gap heat transfer coefficient h_g is found according to

$$\begin{aligned} h_g &= h_0, \quad d \leqslant d_0 \\ h_g &= \frac{1}{\dfrac{d}{k_{air}} + R_c} + h_{rad}, \quad d_0 < d \end{aligned} \tag{28}$$

where d is the gap size, d_0 is the critical gap size (taken to be 0.1 mm in this work), k_{air} is the thermal conductivity of the gas in the gap, R_c is the contact resistance of the interface, h_{rad} is the effective heat transfer coefficient due to radiation, and h_0 is the gap heat transfer coefficient corresponding to a gap of size d_0. Values of these terms, which vary with temperature, and further details of this gap heat transfer calculation are given elsewhere [46, 47]. Truncating the gap heat transfer coefficient at h_0 also facilitates comparison of the different models, forcing the coefficient

DOI: 10.1002/nme

to be constant for small gaps (less than d_0) in order to avoid changes in heat transfer due to minor changes in contact convergence.

Two-way coupling is necessary to capture the effects of the evolving interfacial gap, given that the stress solution depends on the temperature field through thermal strain, Equation (27), and h_g depends on the gap distance calculated from the mechanical solution using Equation (28). Both of the methods presented here incorporate this coupling (see Section 2) using a single finite element type of the CPExT and C3DxT ABAQUS element families in two and three dimensions, respectively.

The liquid steel inside the solidified shell exerts a pressure on the inside surface of the shell, known as the ferrostatic pressure (analogous to hydrostatic pressure), that increases linearly with distance below the liquid steel meniscus. This effect is included in the model as a distributed load applied outward at the surface of the steel shell. This slight shift in the location where the pressure is applied has a negligible effect on the mechanical behavior of the steel shell in the mold, yet greatly improves convergence by avoiding the need to transmit force through the weak elements near the solidification front.

The initial temperature of the simulated steel is uniformly 1540°C, equal to the temperature at which it is poured into the mold. The mold is maintained at a constant 150°C throughout the analysis, which is the approximate average value of the surface temperature in the mold.

5. 2D BILLET-CASTING EXAMPLE

A 2D transverse slice of a billet mold and solidifying shell was used to compare the explicit and implicit methods for the first time on a realistic solidification problem. The models in Figure 6 take advantage of the eight-fold symmetry provided by the billet mold geometry and use identical meshes of standard four-node plane-strain quadrilateral finite elements. The mesh consists of 7686 elements with 15 986 nodes. The element size (edge length) for the strand domain varies from 0.25 mm close to the contact surface to 0.6 mm at the free liquid surface. Owing to the relatively small number of DOF, parallel processing was not investigated in this example.

These models simulate the first 17 s below the meniscus, which corresponds to a 0.71 m long mold with a casting speed of 2.5 m/min. The implicit solver typically required four global NR iterations to achieve global convergence in a given time step, though early times required more than 12 iterations and the adaptive time-stepping algorithm in ABAQUS reduced the time step size. The time steps increased from 10^{-4} to 0.01 s toward the end of the simulation. The implicit analysis required 18 min to complete the simulation on a Dell PowerEdge 1955 server. The explicit code finished the same simulation in 16 min with the variable mass scaling keeping the desired 2×10^{-5} s time steps.

Temperature contours from the two analyses are compared in Figure 7 at the end of the simulation. The temperature drops very near the corner due to the 2D cooling effect in this region. Temperature increases in the off-corner region, owing to the increase in interfacial resistance caused by the gap as the corner shrinks away from the mold. An excellent match between temperature contours from the two methods can be observed.

Contours of y-stress, which is the stress component perpendicular to the solidification direction, are compared at mold exit (17 s) in Figure 8. The results qualitatively agree with the analytical solution, which exhibits surface compression and sub-surface tension near the solidification front. The lowest y-stress of -3.6 MPa is found at the shell surface area where the 'cold' part of the

DOI: 10.1002/nme

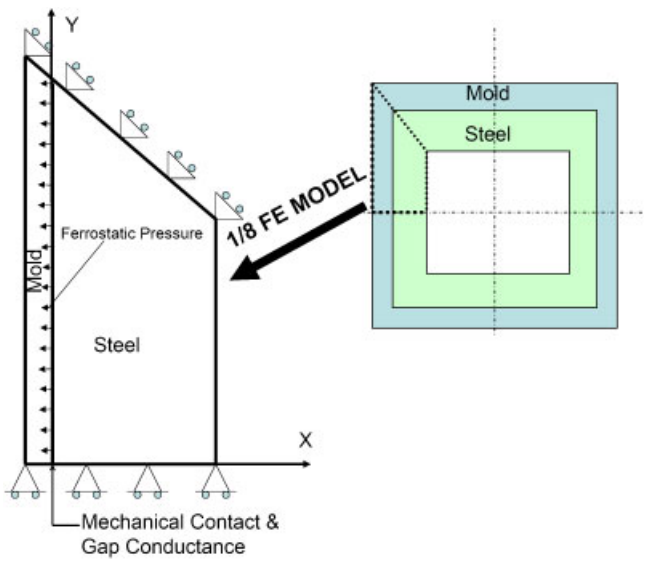

Figure 6. One-eighth billet finite element domain.

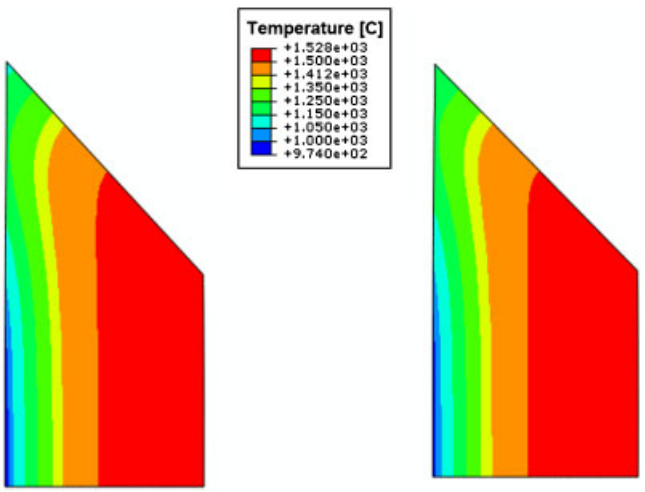

Figure 7. Temperature contour, comparison of 2D implicit and explicit simulations of billet casting (17 s below meniscus).

solidified shell is compressed due to the increased surface shrinkage. The large island of tensile stress whose peak reaches about 1.75 MPa is found in both solutions at the warmest part of newly solidified shell. The implicit solution shows intermittent jagged contours, due to numerical

DOI: 10.1002/nme

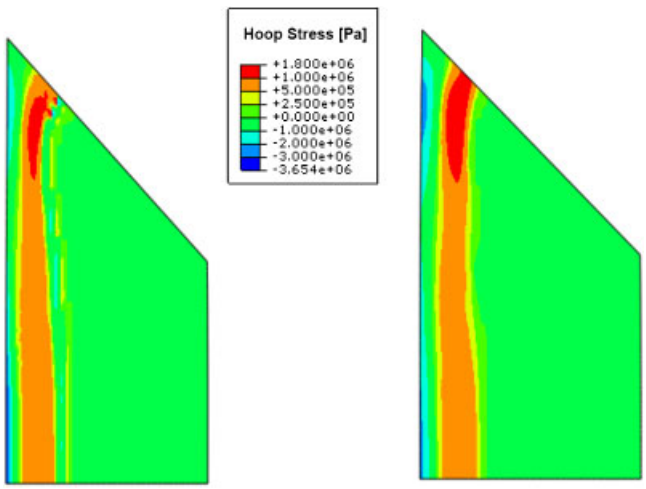

Figure 8. *y*-Stress contour, comparison of 2D implicit and explicit simulations of billet casting (17 s below meniscus).

oscillations. These have been noted in previous work with implicit models [13]. The explicit solution shows smoother contours, which is consistent with its greater stability.

6. FUNNEL-MOLD CASTING

The two thermo-mechanical models were next applied to coupled analyses of continuous casting in a complex-shaped funnel mold. This problem presents a serious computational challenge, especially when treated in three dimensions [20]. Figure 9 shows a schematic of the funnel-mold thin-slab casting process. To enable a thinner mold than conventional slab casting, the funnel shape design provides the space needed for the submerged entry nozzle, which protects the molten steel from atmospheric contamination. This particular funnel design has flat, parallel sections in the center of the mold and near the narrow faces. The funnel section gradually tapers down the mold into a rectangular section, which gives the slab its near-final shape. The dimensions of the funnel mold are shown in Figure 10, which also highlights the computational domain that takes advantage of quarter symmetry. Both the 2D and 3D models are constructed to model 5 s of casting, with a casting speed of 5.5 m/min, which corresponds to 460 mm of the 1100-mm mold length.

6.1. 2D model

The 2D analysis domain described in Section 4 for the funnel mold consists of a thin L-shaped slice that is 17-mm thick in the transverse plane, as shown in Figure 11. This enables simulations of solidification up to almost twice the expected shell thickness at mold exit. To fairly compare the implicit and explicit analyses, both models used meshes consisting of a single layer of hexahedron elements, 2-mm thick in the casting direction. The generalized plane strain condition was imposed with constraint equations because ABAQUS/Explicit currently does not have generalized plane strain elements. All boundary conditions, initial conditions, material properties, and constitutive

DOI: 10.1002/nme

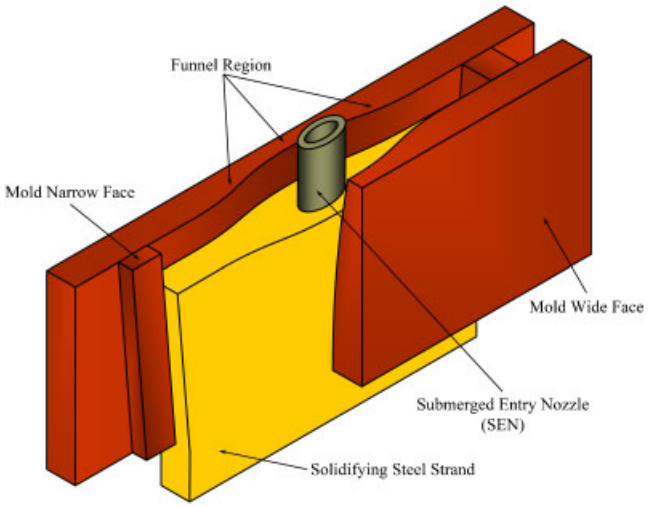

Figure 9. 3D schematic of thin-slab casting.

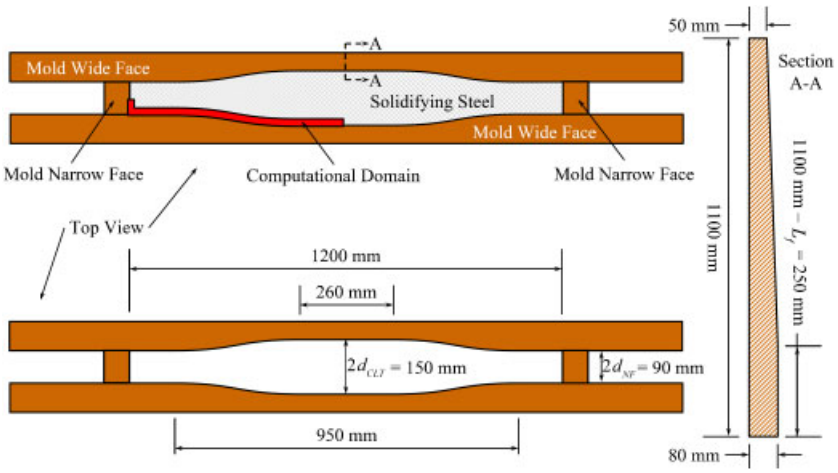

Figure 10. Funnel-mold dimensions.

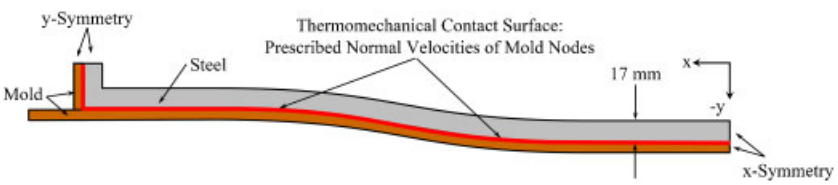

Figure 11. 2D funnel model boundary conditions.

DOI: 10.1002/nme

laws used in both models are the same, as described in Section 4 and illustrated in Figure 11. The shell domain initially corresponds to the shape of the funnel mold at the meniscus. The deformation of the shell caused by moving down through the funnel shape was imposed by prescribing the y-velocities of the mold contact surfaces to appropriate functions of time and space.

A mesh of 29 169 elements (about 160 000 DOF) was chosen to capture the solidification phenomena for this problem. The implicit coupled solver experienced instabilities with its contact algorithm that frequently terminated the simulation, especially at early times. Contact stabilization in the form of viscous damping in the normal direction had to be applied to enable the implicit solver to complete a simulation. The explicit simulation required time steps of 5×10^{-6} s to avoid divergence problems.

The explicit and implicit simulation results at 5 s (460 mm below the meniscus) are compared in Figures 12–15 for the same coarse mesh of 29 169 elements. In addition, a more refined mesh of 109 224 elements (about 543 000 DOF) was investigated for the explicit model to try to attenuate some of the numerical fluctuations.

Figures 12 and 13 show through-thickness profiles of temperature and tangential stress at the mold centerline. Tangential stress (perpendicular to the dendrite growth direction) was computed during post-processing from the 2D stress transformation equation [48] applied to the in-plane stress components. The angle of rotation is readily determined through the geometry of the mold. The explicit and implicit solutions match temperature results within 0.5°C for identical meshes. The refined mesh with the explicit solver produces a smoother temperature profile. The explicit solutions predict less compressive stress on the surface than the implicit solution, and are also unable to capture the sub-surface tensile stress peak that the implicit solution predicts. The more refined explicit solution matches closer to the implicit solution.

Figure 14 shows the surface temperature distribution on the wide face at 5 s below meniscus. The course-mesh explicit and implicit results generally match within about 0.5°C, and the refined mesh is about 2°C hotter. The funnel has a very slight 2D effect on the heat transfer, causing a small (about 1°C) decrease and increase from 130 to 302.5 and 302.5 to 475 mm, respectively, from the centerline.

A small spike in the profiles around 475 mm from the centerline is caused by a small gap opening from a combination of the shell shrinking and the changing funnel shape pushing on the shell. This temperature difference augments the corresponding spike in the surface tangential stress as seen in Figure 15. The spike is more severe with the explicit model, owing to the large wave speed gradients.

The funnel pushes the shell to 'unbend' it, which alters the stress in the funnel region [49]. Although the bending stresses are most severe at the shell surface, the shell experiences compression through its entire thickness, which is partly due to squeezing by the narrow face of the mold. The implicit solution grows more compressive in the outer half of the mold. The differences between the implicit and explicit stress solutions are likely due to the different effects of mesh resolution on the different formulations, as well as the different contact algorithms used.

6.2. 3D model

The final analysis is a 3D explicit Lagrangian simulation of a portion of the shell as it moves through the funnel mold. This model geometry is an extrusion of the 2D domain for a length, ℓ, of 100 mm in the casting direction, and each point in the material has its own 'local time' based on when the point passes the meniscus. The changing shape of the mold face is included in the

DOI: 10.1002/nme

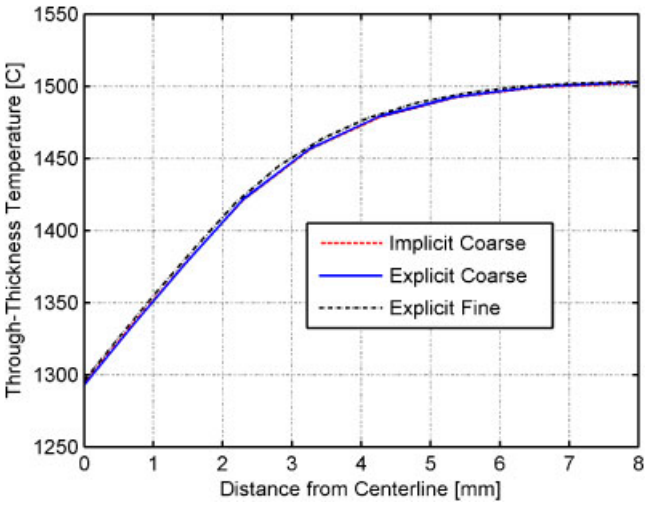

Figure 12. Through-thickness temperature profiles.

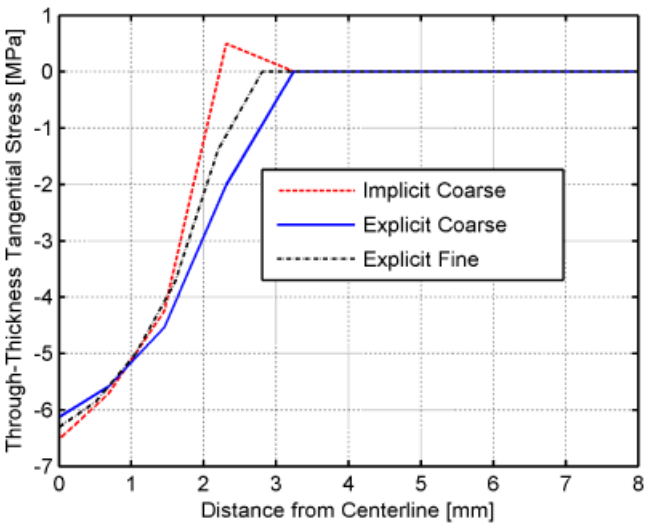

Figure 13. Through-thickness tangential stress profiles.

model by means of a time- and spatially dependent displacement function. Figure 16 shows the boundary conditions on the analysis domain in the Lagrangian frame of reference.

The bottom of the domain begins at the meniscus, and the top was chosen to coincide with the top of the mold, as shown in Figure 16. At $t=0$, the Lagrangian frame begins moving with constant velocity V_C in the Z- (casting) direction. Thus, the distance of any point in the domain below the top of the mold in the lab frame, Z, is related to its distance below the top of the 3D

DOI: 10.1002/nme

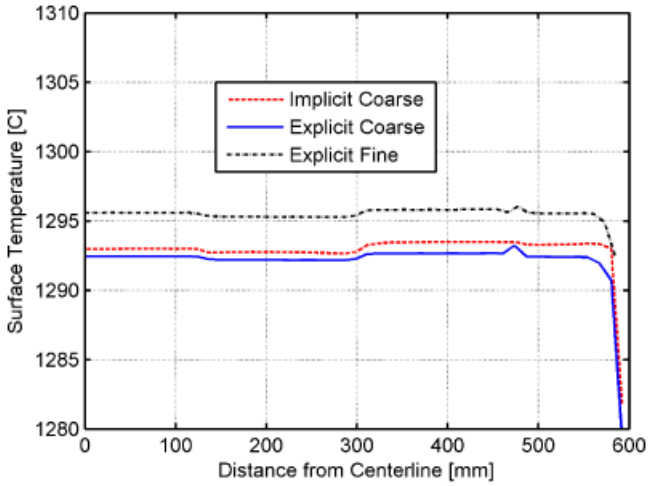

Figure 14. Wide face surface temperature.

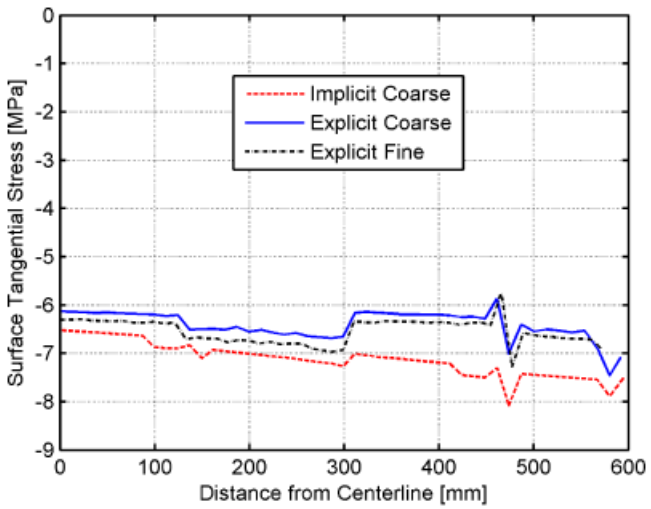

Figure 15. Wide face surface tangential stress.

domain, z, by the following relation, which is simplified in this case because $z_{\text{mensicus}} = \ell$

$$Z = V_C t + z_{\text{meniscus}} + z - \ell = V_C t + z \tag{29}$$

Note that the top of this domain trails the bottom in time by ℓ / V_C, which is 1.09 s in this case. The position of the mold surface at the center of the wide face is given as a function of distance

DOI: 10.1002/nme

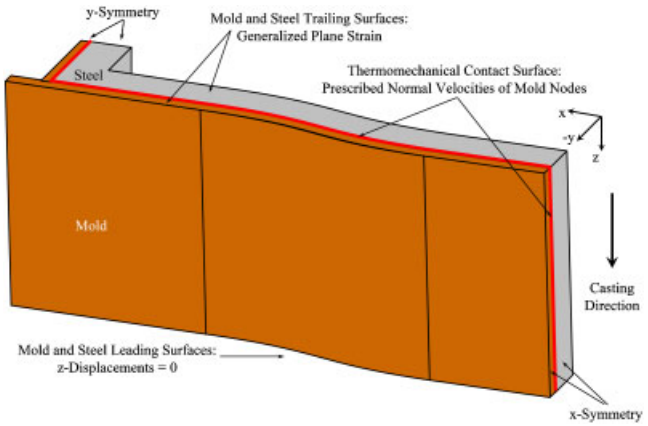

Figure 16. 3D funnel model boundary conditions.

down the mold from Figure 10, as

$$y(Z) = d_{\mathrm{NF}} + (d_{\mathrm{CLT}} - d_{\mathrm{NF}}) \left(1 - \frac{Z}{L_{\mathrm{f}}}\right) \tag{30}$$

where d_{NF} and d_{CLT} are the strand thickness at the narrow face and centerline of the mold on the top surface, respectively, and L_{f} is the funnel length, as shown in Figure 10. Substituting Equation (1) into Equation (2) and taking the first time derivative provides the velocity of each node on this path down the mold surface:

$$v_y(t) = V_{\mathrm{C}} \frac{d_{\mathrm{CLT}} - d_{\mathrm{NF}}}{L_{\mathrm{f}}} \tag{31}$$

Similar expressions are derived for all locations around the mold perimeter, though in general they are functions of x and t.

Typical 3D results from the explicit model are shown in Figure 17. Surface temperatures are relatively uniform, except very near the corner, where 2D cooling exists. This is because the shell stays in reasonably close contact with the surface, so the gaps are all within the tolerance of 0.2 mm, which causes no change in heat conduction. The axial stress (in the casting direction) is one of the primary reasons for applying a 3D model. The relatively uniform stress distribution in the central region indicates that the funnel does not cause significant axial bending in top portions of this mold. Figure 17 clearly shows the complicated 3D state of stress that exists in the corner and off-corner regions, which the 2D models cannot capture correctly. This region is prone to transverse surface cracks in practice, caused by the axial stress.

The 2D and 3D model predictions are compared in Figures 18–21. Near the leading (bottom) and trailing (top) ends of the 3D model domain, 'end effects' significantly alter the stress results. This is due to the lack of constraint, and extends about 15 mm. To make a realistic comparison, data were extracted from the 3D model in a plane 19 mm above the leading edge at 5 s into the simulation (relative to the leading edge). The corresponding 2D results are taken at 4.8 s into the simulation. The models match favorably, as seen in Figures 18–21.

DOI: 10.1002/nme

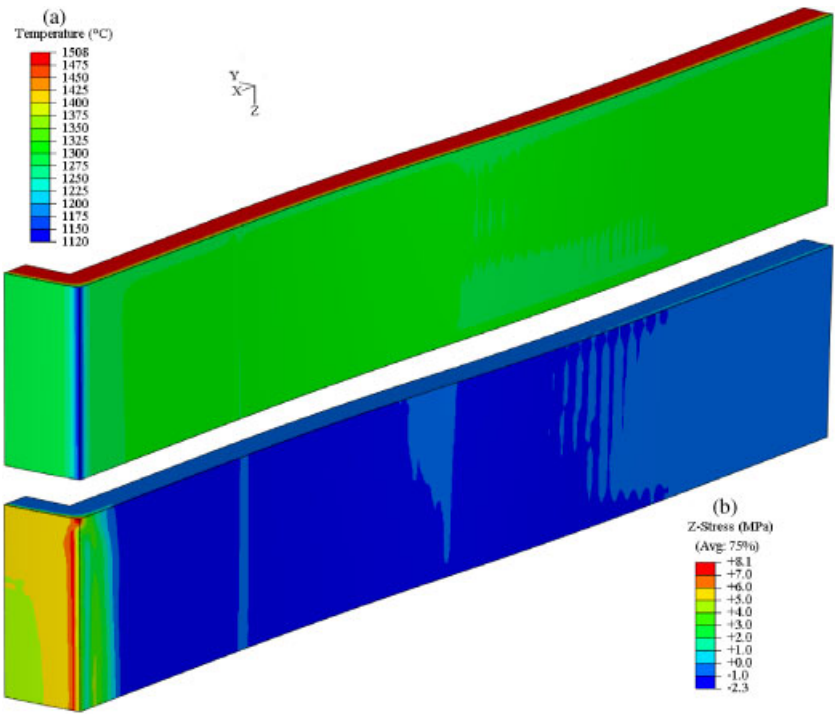

Figure 17. 3D surface contours at 5 s of: (a) temperature and (b) z-stress (casting direction) predicted by the explicit model.

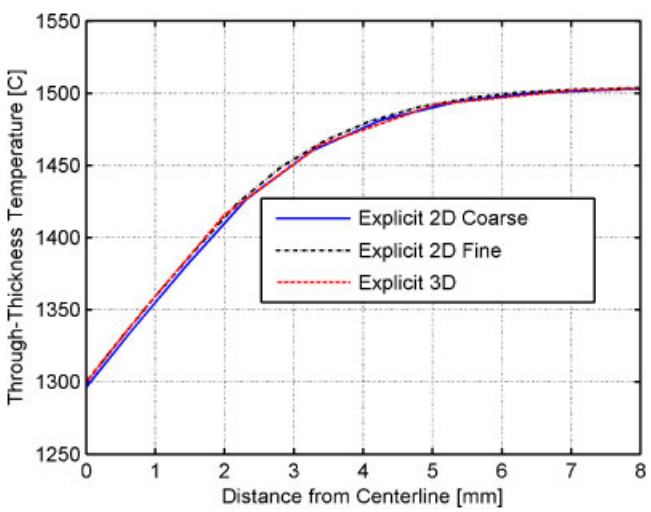

Figure 18. Through-thickness temperature profiles.

DOI: 10.1002/nme

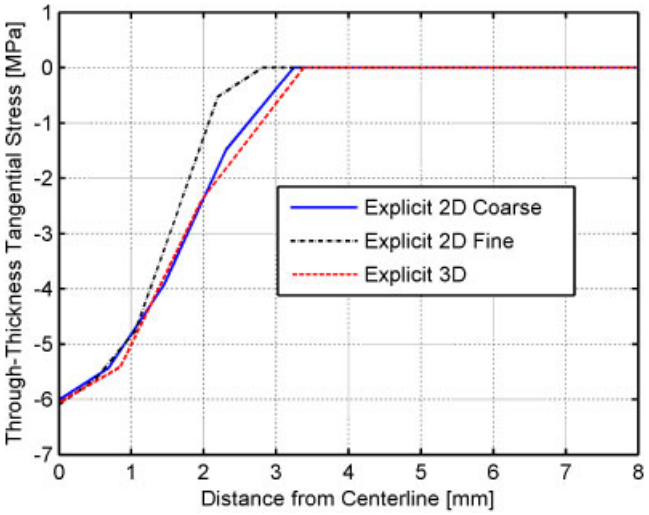

Figure 19. Tangential stress profiles through the shell thickness.

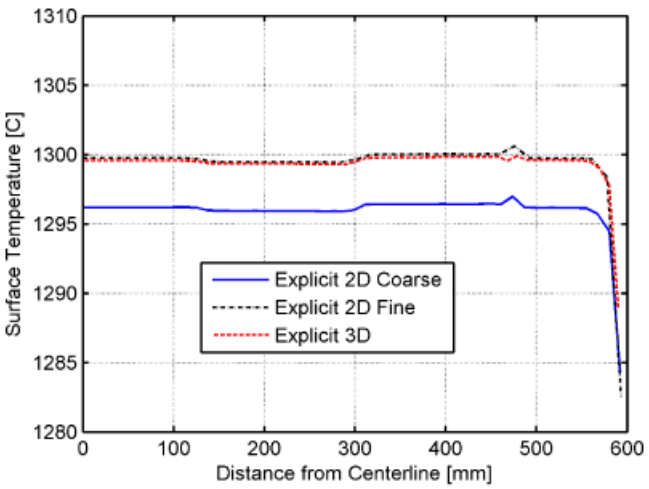

Figure 20. Comparison of model dimensions and mesh refinement on surface temperature.

The temperature profiles through the thickness (Figure 18) and along the perimeter (Figure 20) both match within about 3°C. This agreement validates the arguments made by many previous modelers that axial conduction is negligible with the large Péclet number of this continuous casting process. The 3D model stress results also match reasonably with the 2D predictions of tangential stress (generally within 0.5 MPa) both through the thickness (Figure 19) and along the perimeter (Figure 21). The 3D mesh refinement is the coarsest, which explains the slight variations between the three solutions. The agreement between these models validates the use of the generalized plane

DOI: 10.1002/nme

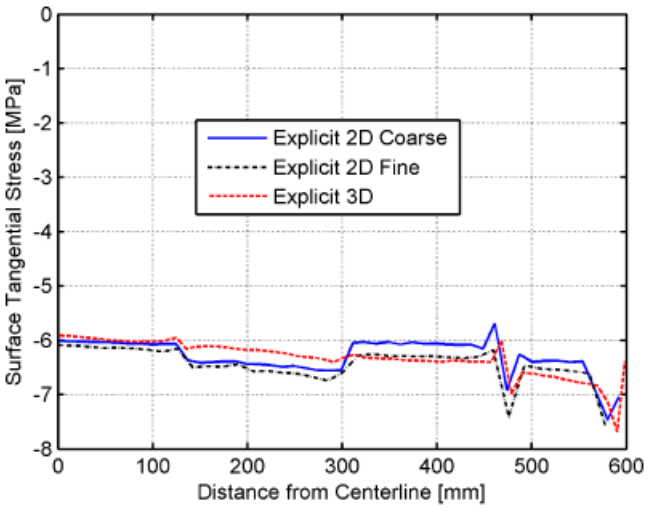

Figure 21. Comparison of model dimensions and mesh refinement on surface tangential stress predictions along shell perimeter.

strain condition in 2D modeling of mechanical behavior of the shell in the mold, in the absence of axial bending.

6.3. Computational performance

The performance of the explicit and implicit methods for the 2D funnel-mold problem was evaluated for different mesh refinements and different numbers of parallel processor cores. Figure 22 presents a comparison of single-core CPU solution times for 0.1 s of simulation as mesh refinement increases from 20 000 to 500 000 degrees of freedom (DOF). The CPU times were normalized relative to the CPU time needed for the smallest 20k DOF mesh refinement (23 s). The two methods have practically the same efficiency for problem sizes less than about 100 000 DOF. As problem size increases past this threshold, the explicit solver out performs the implicit solver at an increasing rate. The corresponding log–log plots are roughly linear and their slopes reveal that CPU time increases in proportion to the number of DOF raised to the power of 1.41 for the explicit model, compared with 1.92 for the less-efficient implicit model. While the scaling exponent for the implicit method, with its direct, sparse-matrix solver, is near to the theoretical value of 2.0 [31], the simple explicit method is less efficient than the expected linearity (1.0) [31], perhaps due to the iteration required for the local integration of the material model. In addition to its large savings in CPU time, the explicit solver required much less memory for all runs: needing on average only 5–10% of the implicit solver memory usage.

Figure 23 compares the wall clock times of the coupled explicit and implicit analyses with multiple cores. The computing platform used in this analysis is a Linux cluster at NCSA made of Dell Power Edge 1955 servers [50], each with two Intel 64 quad-core 2.33 GHz 'Clovertown' processors [51]. The explicit model was run with HP-MPI [52], which allows distributed memory parallel (DMP) jobs between nodes of the cluster via a fast InfiniBand network.

There is only a limited speedup (wall clock scaling) with the implicit solver for 2 and 4 cores. With more than 4 cores, the implicit solver for the 150k-DOF problem experiences a performance

DOI: 10.1002/nme

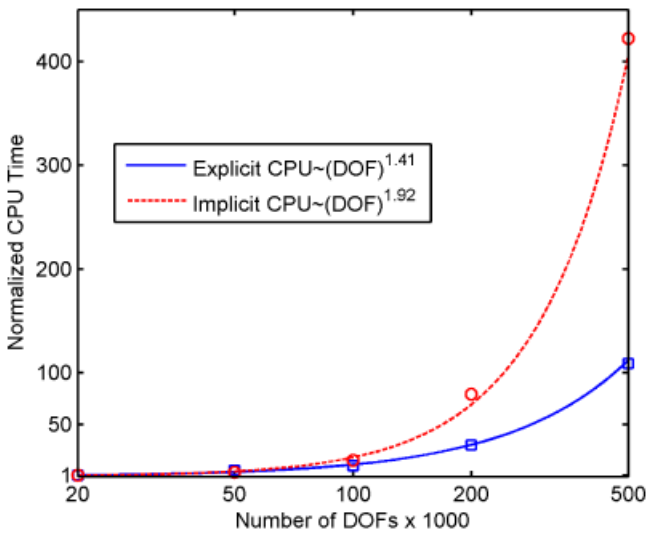

Figure 22. Comparison of CPU time for explicit and implicit models with different domain sizes.

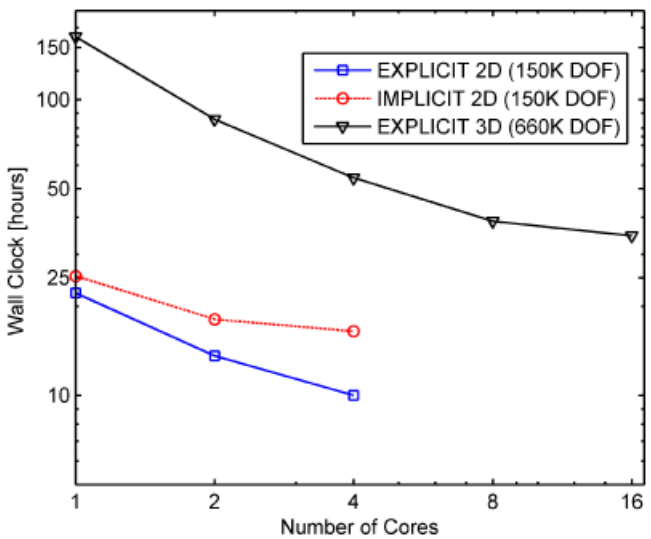

Figure 23. Speedup achieved with parallel processors.

drop, due to increased parallel communication overhead. The explicit solver shows an efficient wall clock scaling from 1 to 4 cores for the 150k-DOF problem, while the larger 660k-DOF problem improved performance even up to 16 cores (2 compute nodes with 8 cores each) before communication performance became an issue. The complete 660k-DOF 3D simulation required 34 h of CPU time on 16 cores (2 nodes) of the Linux cluster.

DOI: 10.1002/nme

The explicit formulation clearly has much more efficient speedup with multiple processors, relative to the implicit formulation. Larger problems, such as 3D domains, solved with the explicit code clearly show an even better speedup with multiple processors.

7. CONCLUSIONS

- An explicit finite element model of steel solidification has been developed using ABAQUS/Explicit.
- This new model includes a VUMAT subroutine, which incorporates the rate-dependent constitutive laws and local integration procedure, based on the UMAT subroutine developed previously for implicit analysis with ABAQUS/Standard [5].
- The temperature and stress results from the explicit model match both the analytical and implicit solutions of the verification problem.
- The explicit and implicit solvers have comparable performance in a 2D problem using a single processor, even though the explicit solver requires very small time steps for numerical stability.
- The explicit solver has demonstrated a high level of robustness when simulating the combined non-linearities coming from the constitutive laws, material properties, and contact conditions that occur during realistic steel-solidification processes.
- The explicit model requires less memory and runs faster than the implicit model for problems with more than 100 000 DOF in either two or three dimensions. Furthermore, the explicit solver also scales better on parallel computers.
- The assumptions of neglecting axial conduction and generalized plane strain (in the absence of axial bending) when modeling continuous casting of steel have been proven valid by direct comparison, for the first time, of the 2D and 3D model results.
- The new, explicit solver-based solidification model presented in this work will be particularly beneficial in future analysis of 3D, fully coupled problems with properly refined meshes on DMP multi-core clusters, which are becoming more commonly available.

NOMENCLATURE

A	surface (m^2)
A_h	convection-prescribed surface (m^2)
A_Φ	traction-prescribed surface (m^2)
$[B]$	spatial derivative of [N] (1/m)
$\mathbf{b}$	volumetric force vector (N)
c_p	specific heat (J/kg K)
c_d	dilatation wave speed (m/s)
$[C]$	capacitance matrix (J/kg)
$\underline{\underline{\mathbf{D}}}$	fourth-order elasticity tensor (N/m^2)
$\overline{d}$	interfacial gap size (m)
d_0	critical gap size (m)
d_CLT	centerline strand thickness (m)
d_NF	narrow face strand thickness (m)

DOI: 10.1002/nme

E	elastic modulus (N/m^2)
f	viscoplastic law function ($1/s$)
fc	empirical constant in Kozlowski III law (MPa^{-f3}/s)
$f_{\delta c}$	empirical constant in enhanced power delta law
f_1	empirical constant in Kozlowski III law (MPa)
f_2	empirical constant in Kozlowski III law
f_3	empirical constant in Kozlowski III
H	enthalpy ($J/kg\,K$)
H_f	latent heat of solidification ($J/kg\,K$)
h_g	total gap heat transfer coefficient ($W/m^2\,K$)
h_0	critical gap heat transfer coefficient ($W/m^2\,K$)
h_{rad}	radiation gap heat transfer coefficient ($W/m^2\,K$)
$\underline{\underline{\mathbf{I}}}$	fourth-order identity tensor
$\mathbf{I}$	second-order identity tensor
$\underline{\underline{\mathbf{J}}}$	material Jacobian (N/m^2)
$[K]$	tangent stiffness matrix (N/m)
k	thermal conductivity (W/mK)
k_{air}	air thermal conductivity (W/mK)
k_B	bulk modulus (N/m^2)
L_e	characteristic element length (m)
L_f	funnel length (m)
ℓ	thickness of 3D domain in casting dir (m)
m, n	empirical constants used power delta law
$[N]$	element shape functions
$\mathbf{n}$	surface unit vector
$[M]$	mass matrix (kg)
$\mathbf{P}$	external force vector (N)
$\hat{q}$	prescribed heat flux (W/m^2)
Q	activation energy constants (K)
$\mathbf{R}_u$	mechanical residual force (N)
$\mathbf{R}_T$	thermal residual force (W)
R_c	contact resistance ($m^2\,K/W$)
$\mathbf{S}$	internal force vector (N)
T	temperature (°C, K)
T_{liq}	liquidus temperature (°C)
T_{sol}	solidus temperature (°C)
T_m	mold temperature (°C)
T_0	reference temperature (°C)
$\mathbf{u}$	displacement vector (m)
$\dot{\mathbf{u}}$	velocity vector (m/s)
$\ddot{\mathbf{u}}$	acceleration vector (m/s^2)
V	volume (m^3)
Vc	casting speed (m/s)
V_y	nodal velocity of mold surface (m/s)
$\mathbf{x}$	position vector (m)

DOI: 10.1002/nme

$y(Z)$	nodal center face mold surface y position (m)
Z	nodal distance below mold top (m)
z	nodal distance below 3D domain top (m)
z_{meniscus}	meniscus distance (m)
α	coefficient of thermal expansion (1/°C)
δ_{ij}	Kronecker's delta
$\boldsymbol{\varepsilon}$	total strain tensor
$\Delta\hat{\boldsymbol{\varepsilon}}$	guess for tot. strain incr. tensor
$\dot{\boldsymbol{\varepsilon}}$	total strain rate tensor (1/s)
$\boldsymbol{\varepsilon}_{\text{el}}$	elastic strain tensor
$\dot{\boldsymbol{\varepsilon}}_{\text{el}}$	elastic strain rate tensor (1/s)
$\boldsymbol{\varepsilon}_{\text{ie}}$	inelastic strain tensor
$\dot{\boldsymbol{\varepsilon}}_{\text{ie}}$	inelastic strain rate tensor (1/s)
$\dot{\overline{\varepsilon}}_{\text{ie}}$	equivalent inelastic strain (1/s)
$\boldsymbol{\varepsilon}_{\text{th}}$	thermal strain tensor
$\dot{\boldsymbol{\varepsilon}}_{\text{th}}$	thermal strain rate tensor (1/s)
λ	first Lamé elastic constant (N/m^2)
μ	shear modulus (N/m^2)
$\boldsymbol{\sigma}$	stress tensor—small-strain formulation (N/m^2)
$\overline{\sigma}$	equivalent stress (N/m^2, MPa)
ρ	density (kg/m^3)
μ	shear modulus (N/m^2)
$\boldsymbol{\Phi}$	surface traction vector (N/m^2)
$\omega_{\max}$	highest system frequency (1/s)

ACKNOWLEDGEMENTS

The authors would like to thank the National Center for Supercomputing Applications at the University of Illinois at Urbana-Champaign (UIUC) for computational resources, the Continuous Casting Consortium at UIUC, the National Science Foundation (Grant CMMI-07-27620), and Corus Steel in IJmuiden, The Netherlands.

REFERENCES

1. Thomas BG, Sengupta J. The visualization of defect formation during casting processes. *JOM—The Minerals Metals and Materials Society* 2006; **58**(12):16–18.
2. Hattel JP, Hansen N, Hansen LF. Analysis of thermal induced stresses in die casting using a novel control volume FDM-technique. *Proceedings Modeling of Casting Welding and Advanced Solidification Process VI*, Palm Coast, FL, 21–26 March 1993.
3. Taylor G, Bailey C, Cross M. Solution of elasto/visco plastic equations: a finite volume approach. *Applied Mathematical Modeling* 1995; **19**:746–760.
4. Lee J, Yeo T, OH KH, Yoon J, Yoon U. Prediction of cracks in continuously cast steel beam blank through fully coupled analysis of fluid flow, heat transfer, and deformation behavior of a solidifying shell. *Metallurgical and Materials Transactions A* 2000; **31A**:225–237.
5. Koric S, Thomas BG. Efficient thermo-mechanical model for solidification processes. *International Journal for Numerical Methods in Engineering* 2006; **66**:1955–1989.
6. Grill A, Brimacombe JK, Weinberg F. Mathematical analysis of stress in continuous casting of steel. *Ironmaking and Steelmaking* 1976; **3**:38–47.

DOI: 10.1002/nme

7. Kelly JE, Michalek KP, O'Connor TG, Thomas BG, Dantzig JA. Initial development of thermal and stress fields in continuously cast steel billets. *Metallurgical Transactions A* 1988; **19A**(10):2589–3602.
8. Kristiansson JO. Thermomechanical behavior of the solidifying shell within continuous casting billet molds—a numerical approach. *Journal of Thermal Stresses* 1984; **7**:209–226.
9. Williams JR, Lewis RW, Morgan K. An elastic–viscoplastic thermal stress model with applications to the continuous casting of metals. *International Journal for Numerical Methods in Engineering* 1979; **14**:1–9.
10. Boehmer JR, Funk G, Jordan M, Fett FN. Strategies for coupled analysis of thermal strain history during continuous solidification processes. *Advances in Engineering Software* 1998; **29**(7–9):679–697.
11. Farup I, Mo A. Two-phase modeling of mushy zone parameters associated with hot tearing. *Metallurgical and Materials Transactions* 2000; **31**:1461–1472.
12. Zhu H. Coupled thermal–mechanical finite-element model with application to initial solidification. *Ph.D. Thesis*, University of Illinois, 1993.
13. Chunsheng L, Thomas BG. Thermo-mechanical finite-element model of shell behavior in continuous casting of steel. *Metallurgical and Materials Transactions B* 2005; **35B**(6):1151–1172.
14. Tan L, Zabaras N. A thermomechanical study of the effect of mold topography on the solidification aluminum alloys. *Materials Science and Engineering* 2005; **404**(1–2):197–207.
15. Belet M, Fachinotti VD. ALE method for solidification modeling. *Computational Methods in Applied Mechanics and Engineering* 2004; **193**:4355–4381.
16. Risso JM, Huespe AE, Cardona A. Thermal stress evaluation in the steel continuous casting process. *International Journal for Numerical Methods in Engineering* 2006; **65**(9):1355–1377.
17. Lewis RW, Postek EW, Han Z, Gethin DT. A finite element model of squeeze casting process. *International Journal of Numerical Methods for Heat and Fluid Flow* 2006; **16**(5):539–572.
18. Pascon F, Habraken AM. Finite element study of the effect of some local defects on the risk of transverse cracking in continuous casting of steel slabs. *Computational Methods in Applied Mechanics and Engineering* 2007; **196**:2285–2299.
19. Li C, Thomas BG. Maximum casting speed for continuous cast steel billets based on sub-mold bulging computation. *85th Steelmaking Conference Proceedings ISS-AIME*, Nashville, TN, 2002; 109–130.
20. Koric S, Thomas BG. Thermo-mechanical model of solidification processes with ABAQUS. *ABAQUS Users Conference* (*2007*), Paris, France, 2007; 320–336.
21. Taylor L, Cao J, Karafillis AP, Boyce MC. Numerical simulations of sheet-metal forming. *Journal of Materials Processing Technology* 1995; **50**:168–179.
22. Kutt LM, Pifko AB, Nardiello JA, Papazian JM. Low-dynamic finite element simulation of manufacturing processes. *Computers and Structures* 1998; **66**:1–17.
23. Ristic S, He S, Van Bael A, Van Houtte P. Texture-based explicit finite element analysis of sheet metal forming. *Materials Science Forum* 2005; **495–497**:1353–1540.
24. Rebelo N, Nagtegaal JC, Taylor LM, Passman R. Comparison of implicit and explicit methods in the simulation of metal forming processes. *Numerical Methods in Industrial Forming Processes-Numiform 92*, Valbonne, France, 1992; 99–108.
25. Harewood FJ, McHugh PE. Comparison of implicit and explicit finite element methods using crystal plasticity. *Computational Materials Science* 2007; **39**:481–494.
26. Lewis RW, Morgan K, Thomas HR, Seetharamu KN. *The Finite Element Method in Heat Transfer Analysis*. Wiley: New York, 1996.
27. Thomas BG, Brimacombe JK, Samarasekera IV. The formation of panel cracks in steel ingots, a state of the art review. Part I—hot ductility of steel. *Transactions of the Iron and Steel Society* 1986; **7**:7–20.
28. Mase GE, Mase GT. *Continuum Mechanics for Engineers* (2nd edn). CRC Press: Boca Raton, FL, 1999.
29. Zienkiewicz OC, Taylor RL. *Finite Element Method*: *Solid and Fluid Mechanics Dynamics and Non-Linearity*. McGraw-Hill: New York, 1991.
30. Felippa CA, Park KC. Staggered transient analysis procedures for coupled mechanical systems: formulation. *Computer Methods in Applied Mechanics and Engineering* 1980; **24**:61–111.
31. *ABAQUS User Manuals v6.7*. Simulia Inc., 2007.
32. Weiner JH, Boley BA. Elastic–plastic thermal stresses in a solidifying body. *Journal of the Mechanics and Physics of Solids* 1963; **11**:145–154.
33. Koric S, Thomas BG. Thermo-mechanical models of steel solidification based on two elastic visco-plastic constitutive laws. *Journal of Materials Processing Technology* 2008; **197**:408–418.
34. Kozlowski PF, Thomas BG, Azzi JA, Wang H. Simple constitutive equations for steel at high temperature. *Metallurgical Transactions* 1992; **23A**:903–918.

DOI: 10.1002/nme

35. Wray PJ. Effect of carbon content on the plastic flow of plain carbon steels at elevated temperatures. *Metallurgical Transactions A* 1982; **13A**:125–134.
36. Suzuki T, Tacke KH, Wunnenberg K, Schwerdtfeger K. Creep properties of steel at continuous casting temperatures. *Ironmaking and Steelmaking* 1988; **15**(3):90–100.
37. Brandes EA. *Smithell's Metals Reference Book* (6th edn). Butterworth: Boston, 1983.
38. Lush AM, Weber G, Anand L. An implicit time-integration procedure for a set of integral variable constitutive equations for isotropic elasto-viscoplasticity. *International Journal of Plasticity* 1989; **5**:521–549.
39. Zabaras N, Arif ABFM. A family of integration algorithms for constitutive equations in finite difference deformations elasto-viscoplasticity. *International Journal for Numerical Methods in Engineering* 1992; **33**:59–84.
40. Crisfield MA. *Nonlinear FEA of Solids and Structures*. Wiley: New York, 1991.
41. Mizukami H, Murakami K, Miyashita Y. Elastic modulus of steels at high temperature. *Journal of the Iron and Steel Institute of Japan* 1977; **63**(146):S-652.
42. Harste K. Investigation of the shrinkage and the origin of mechanical tension during the solidification and successive cooling of cylindrical bars of Fe–C alloys. *Ph.D. Dissertation*, Technical University of Clausthal, 1989.
43. Harste K, Jablonka A, Schwerdtfeger K. Shrinkage and formation of mechanical stresses during solidification of round steel strands. *4th International Conference on Continuous Casting*, Brussels, Belgium, vol. 2, 1988; 633–644.
44. Jimbo I, Cramb AW. The density of liquid iron–carbon alloys. *Metallurgical Transactions B* 1993; **24B**(1):5–10.
45. Meng Y, Thomas BG, Polycarpou AA, Prasad A, Henein H. Mold slag property measurements to characterize continuous-casting mold–shell gap phenomena. *Canadian Metallurgical Quarterly* 2006; **45**(1):79–94.
46. Park JK, Thomas BG, Samasekera IV. Analysis of thermomechanical behavior in billet casting with different mould corner radii. *Ironmaking and Steelmaking* 2002; **29**.
47. Han HN, Lee JE, Yeo TJ, Won YM, Kim K, Oh KH, Yoon JK. A finite element model for 2-dimensional slice of cast strand. *ISIJ International* 1999; **39**(5):445–455.
48. Ugural AC, Fenster SK. *Advanced Strength and Applied Elasticity* (4th edn). Prentice-Hall: Englewood Cliffs, NJ, 2003.
49. Hibbeler LC, Thomas BG, Santillana B, Hamoen A, Kamperman A. Longitudinal face crack prediction with thermo-mechanical models of thin-slabs in funnel moulds. *6th European Conference on Continuous Casting*, Riccione, Italy, 3–6 June 2008.
50. Dell Power Edge 1955 server product details. Dell Inc., 2007.
51. Intel Xeon 5300 quad core processor. Intel Inc., 2007.
52. *HP-MPI User's Guide* (11th edn). Hewlett-Packard Company, 2007.

DOI: 10.1002/nme